International Journal of Solids and Structures 55 (2015) 66–78

Contents lists available at ScienceDirect

International Journal of Solids and Structures

journal homepage: www.elsevier.com/locate/ijsolstr

Global sensitivity analysis in the identification of cohesive models using full-field kinematic data

Marco Alfano [a,b,c,*], Gilles Lubineau [b], Glaucio H. Paulino [c]

[a] Department of Mechanical, Energy and Management Engineering, University of Calabria, Via P. Bucci 44C, 87036 Rende, CS, Italy
[b] King Abdullah University of Science and Technology, Physical Sciences and Engineering Division, COHMAS Laboratory, Thuwal 23955-6900, Saudi Arabia
[c] Department of Civil and Environmental Engineering, University of Illinois at Urbana-Champaign, 205 N. Matthew Avenue, Urbana, IL 61801, USA

ARTICLE INFO

Article history:
Received 22 January 2014
Received in revised form 3 May 2014
Available online 14 June 2014

Keywords:
Cohesive zone model
Identification
Double Cantilever Beam
Sensitivity analysis
Sobol indexes

ABSTRACT

Failure of adhesive bonded structures often occurs concurrent with the formation of a non-negligible fracture process zone in front of a macroscopic crack. For this reason, the analysis of damage and fracture is effectively carried out using the cohesive zone model (CZM). The crucial aspect of the CZM approach is the precise determination of the traction-separation relation. Yet it is usually determined empirically, by using calibration procedures combining experimental data, such as load–displacement or crack length data, with finite element simulation of fracture. Thanks to the recent progress in image processing, and the availability of low-cost CCD cameras, it is nowadays relatively easy to access surface displacements across the fracture process zone using for instance Digital Image Correlation (DIC). The rich information provided by correlation techniques prompted the development of versatile inverse parameter identification procedures combining finite element (FE) simulations and full field kinematic data. The focus of the present paper is to assess the effectiveness of these methods in the identification of cohesive zone models. In particular, the analysis is developed in the framework of the variance based global sensitivity analysis. The sensitivity of kinematic data to the sought cohesive properties is explored through the computation of the so-called Sobol sensitivity indexes. The results show that the global sensitivity analysis can help to ascertain the most influential cohesive parameters which need to be incorporated in the identification process. In addition, it is shown that suitable displacement sampling in time and space can lead to optimized measurements for identification purposes.

1. Introduction and motivation

Interfaces play a significant role on the overall mechanical performance of adhesive bonded joints in a variety of applications, including aerospace, electronics, construction and solar energy (Adams et al., 1997; Kinloch, 1987; Sridharan, 2008). These structures show a rich array of potential fracture mechanisms, but interfacial debonding of the adjacent layers is the most widely encountered in actual applications (Sridharan, 2008). Interfacial adhesion, and in turn susceptibility to debonding, is intimately connected to sources of energy dissipation occurring at different length-scales, such as the breakage of intrinsic adhesion forces at the nano-scale (e.g., primary bonds and physical interactions), micro-scale fibrillation in the vicinity of the crack tip (van den Bosch et al., 2008), and macro scale bulk plasticity in the bonded substrates (Alfano et al., 2011). As a result joint failure often occurs concurrent with the development of large scale bridging (or cohesive) zone. In these circumstances, the magnitude of cohesive tractions across the adhesive layer plays a significant role on the overall deformation of the system and the small scale yielding conditions breaks down. Since linear elastic fracture mechanics is no longer fully adequate (Cavalli and Thouless, 2001), the analysis of damage and fracture in adhesive bonded structures is effectively carried out using the cohesive zone model (CZM) (Dugdale, 1960; Barenblatt, 1962).

Several recent contributions, which reviewed advantages and limitations of the CZM approach, have highlighted that the crucial aspect of the methodology is the determination of the traction-separation relation[1] Park and Paulino, 2013. This theme has been vigorously pursued in recent times. Earlier works focused on semi-empirical calibration procedures combining experimental testing

* Corresponding author at: Department of Mechanical, Energy and Management Engineering, University of Calabria, Via P. Bucci 44C, 87036 Rende, CS, Italy. Tel.: +39 (0)984 494156.
E-mail address: marco.alfano@unical.it (M. Alfano).

[1] The link between cohesive interaction and opening displacements.

http://dx.doi.org/10.1016/j.ijsolstr.2014.06.006
0020-7683/

performed on beam-like adhesive bonded samples (e.g. Double Cantilever Beam Alfano et al., 2011, End Notch Flexure Lee et al., 2010) and finite element (FE) simulations of fracture. Typical experimental data employed in the calibration include point data, such as the load–displacement curve, sample deflection and crack opening profile (Alfano et al., 2011; Yang et al., 1999; Yang et al., 2001; Yang and Thouless, 2001; Sun et al., 2008; Alfano et al., 2011; Gowrishankar et al., 2012). On the other hand, recent progress in image correlation enabled relatively accurate and low cost measurements of full field kinematic data by using Digital Image Correlation (DIC) (Sutton et al., 2009). A correlation algorithm compares the local features of a pair of digital images searching for the displacement field which provides the best match between pixel intensities. Compared to classical measurement devices (e.g. extensometers), DIC can resolve a very large number of kinematic unknowns. Abanto-Bueno and Lambros (2005) and Tan et al. (2006) employed DIC to measure the displacement field across the fracture process zone in photodegradable copolymers and bulk explosives (PBX 9501), respectively. Model traction separation relations were determined by correlating the calculated opening stress with the measured opening displacements across the fracture plane. Specifically, the crack opening profile was extracted from the measured displacement field, while cohesive tractions were estimated through the derived strain field and bulk constitutive material properties. The usefulness of this method is essentially limited to materials displaying linear elastic bulk behavior; moreover, it is not readily adaptable to bonded samples. Alternative full field techniques could be also employed, however, recent works mostly focused on DIC because it does not require costly hardware or complicated procedures and provides accurate results. Specifically, it is often assumed that when the displacement field is measured by DIC the primary sources of errors are from digital image resolution and the DIC algorithm itself. Image resolution depends on the acquisition device. Usually the quality that can be guaranteed with modern CCD or CMOS sensors, in conjunction with high magnification lens, is in the scale of 10^0–10^2 microns per pixel (Shen et al., 2010). Resolution of the DIC software is measured as a fraction of pixel, and sub-pixel precision can be also achieved. The combined effect can lead to maximum errors in order of tens of microns for accurate measurements, that is quite satisfactory for a reliable determination of cohesive fracture properties (Shen et al., 2010).

The rich information provided by DIC prompted the development of additional inverse techniques. These have been recently reviewed in Avril et al. (2008), and include the finite element model updating method (FEMU), the constitutive equation gap method (CEGM), the virtual fields method (VFM), the equilibrium gap method (EGM) and the reciprocity gap method (RGM). The FEMU approach combines finite element (FE) simulations and full field kinematic data. In this method, a least squares norm, which quantifies the discrepancy between experimental data and the corresponding finite element counterpart, is minimized so as to get the unknown material parameters. This technique was initially deployed in order to identify elastic, elasto- plastic and viscoelastic bulk constitutive material properties (Avril et al., 2008; Pottier et al., 2011; Lubineau, 2009; Florentin and Lubineau, 2010; Blaysat et al., 2012; Moussawi et al., 2013). Subsequently, it was also used to supplement the existing methods for the determination of cohesive fracture properties, see Shen et al. (2010), Shen and Paulino (2011), Gain et al. (2011), Fedele et al. (2009), Valoroso and Fedele (2010) and Fedele and Santoro (2012) to list a few. In these simulation-based identification frameworks, cohesive properties were iteratively adjusted in order to minimize the difference between computed and measured surface displacements across sample surface (Shen and Paulino, 2011; Gain et al., 2011) or a suitable sub-region (Fedele et al., 2009; Valoroso and Fedele, 2010). These works have shown that the determination of cohesive models poses challenges both in terms of measurement and identification. Primarily, the quantity (and quality) of experimental data obtained using DIC have to be carefully taken into account. A large set of data with low sensitivity not only adversely affects the identification process, but also increases the problem size and computational cost owing to the accumulation of unresolved residuals (Valoroso and Fedele, 2010). Therefore, the actual sensitivity of the measured displacement fields to variation of cohesive zone parameters has a key role on the outcome of the identification process.

From this standpoint, the information provided by a sensitivity analysis (SA) may allow one to recognize the most informative measurable quantities (over space and time) for identification purposes. In other words, the results of a SA can be employed to perform an effective time–space displacement sampling which can ultimately improve the whole identification process. Sensitivity analyses can be roughly divided in *local* and *global* analyses (Saltelli et al., 2008). Local sensitivity analyses allow one to study the fluctuations of the output variables as a consequence of small variations of the input data near a given observation point. Local sensitivity analyses have been carried out in previous related works concerning the identification of cohesive zone models in adhesive joints (Fedele et al., 2009; Valoroso and Fedele, 2010; Fedele and Santoro, 2012). However, local SA is not able to explore the whole space of the input factors, but only selected base points. On the other hand, global sensitivity analysis deals with the variability of the output due to the fluctuations of the input data throughout the potential domain of variation – which is often idealized as a hypercube. It is worth noting that in the case of linear problems, local and global approaches provide essentially similar results. However, for highly non linear models the sensitivity can largely vary from point to point and, as a result, a local approach may not be appropriate. In these cases, a global sensitivity analysis prevails over other methods (e.g. sigma-normalized derivatives, standardized regression coefficients, as it is more effective in handling complex non-linear models. The Sobol variance-based global analysis is a very popular global sensitivity analysis method which allows one to quantify the amount of variance that each input parameter (e.g. cohesive strength) contributes to the unconditional variance of the model output (e.g. surface displacements or a suitable *cost function* thereof). The Sobol method makes use of the Monte-Carlo simulation framework to compute sensitivity indexes. The values of the input variables are sampled using a quasi random sequence. If compared to other distributions (e.g. gaussian, uniform), it allows one to explore, in a more uniform fashion, the whole range of variability of the input parameters. With such sampling, a reduced number of model evaluations are needed and a reasonable convergence speed is therefore ensured. In this work, the Sobol method has been employed to perform a sensitivity analysis in the identification of selected cohesive zone models using full field kinematic data. As the focus herein is on mode I fracture, the analysis is carried out considering a model Double Cantilever Beam (DCB). A cost function is defined in terms of the residual between computed and experimental surface displacement data. Displacement data concern a suitable region of interest (ROI) across the fracture process zone which includes portions of the joined substrates close to the adhesive layer. The global sensitivity analysis is carried out to assess the sensitivity of the objective function to displacement sampling in *time* (i.e. selected loading step) and *space* (i.e. size of the ROI). The first order sensitivity indexes (Saltelli et al., 2008) are calculated for the cohesive fracture properties pertaining to various cohesive models, including bilinear, trapezoidal and potential based models (Alfano et al., 2009; Park et al., 2009). The influence of cohesive strength, cohesive energy and other parameters are considered simultaneously. As it will be shown in this paper, selecting the most informative

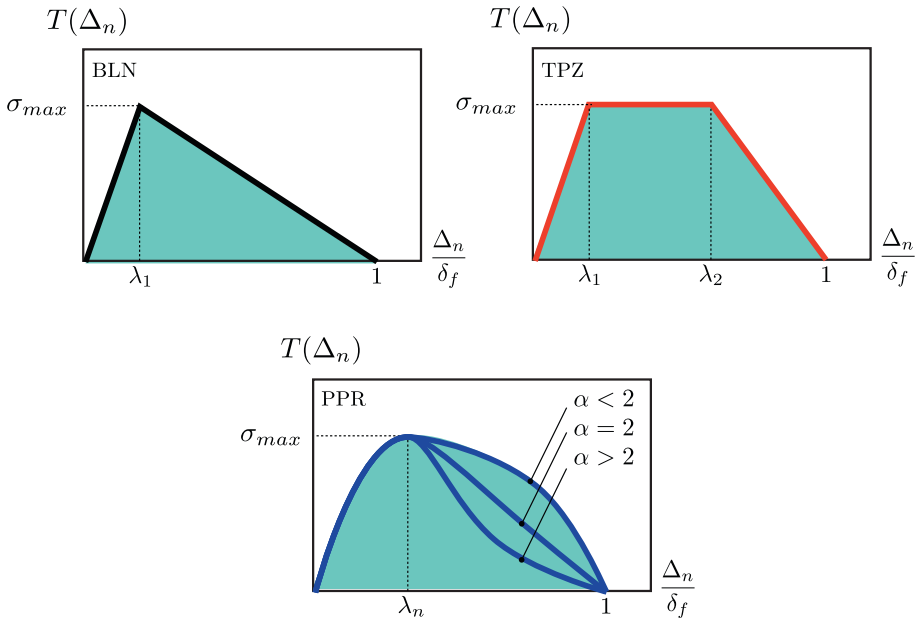

Fig. 1. Fracture boundary conditions for the cohesive zone models employed in the present study (BLN: bilinear model; TPZ: trapezoidal model; PPR: Park–Paulino–Roesler potential based model).

measurable quantities in space and time has a strong influence on the resulting sensitivity indexes.

The paper is organized as follow. Section 2 summarizes the cohesive models analyzed in the paper and provides details concerning the studied cost function. Section 3 briefly introduces the finite element model. Section 4 deals with the identification problem. Section 5 provides the theoretical background on the Sobol global sensitivity analysis approach and its practical implementation. In Section 6 the obtained results are presented and discussed. Finally, Section 7 concludes the paper and provides suggestions for future works.

2. Cohesive models analyzed in the present work

In the cohesive zone model approach, material failure is characterized by a traction-separation relation which links the cohesive traction and the relative displacement across cohesive surfaces. The peak stress and the area enclosed by the traction-separation relation are often referred to as the cohesive strength and cohesive energy, respectively. As reviewed in Park and Paulino (2013), several cohesive constitutive relationships have been proposed in the last several decades. These can be classified as either non potential-based models or potential-based models. Non potential-based cohesive models are relatively simple to develop, because a symmetric system is not required. In the case of potential-based models, the traction-separation relationships across fracture surfaces are obtained from potential functions. In order to perform the sensitivity analysis, classical bilinear and trapezoidal (e.g. Alfano et al., 2009) non potential-based models, as well as the PPR potential-based model (Park et al., 2009) have been considered. The corresponding mode I traction-separation relations, which are displayed in Fig. 1, are now briefly summarized.

2.1. Bilinear model

In the bilinear cohesive model, the evolution of the normal cohesive interaction, $T(\Delta_n)$, with opening displacement, Δ_n, is given as follows:

$$T(\Delta_n) = \begin{cases} \sigma_{max}\frac{\Delta_n}{\lambda_1\delta_f}, & \Delta_n < \lambda_1\delta_f, \quad (1a) \\ \sigma_{max}\frac{\delta_f-\Delta_n}{\delta_f(1-\lambda_1)}, & \lambda_1\delta_f \leqslant \Delta_n < \delta_f, \quad (1b) \\ 0, & \Delta_n \geqslant \delta_f, \quad (1c) \end{cases}$$

where, σ_{max} is the cohesive strength, λ_1 is a parameter which controls the initial slope (i.e. the stiffness) of the model, δ_f is the final opening width,[2] while the area under the traction-separation relation is the cohesive fracture energy, ϕ_n. In turn, there are three independent cohesive parameters that fully define the cohesive interaction: $\mathbf{X}^T = [\phi_n, \sigma_{max}, \lambda_1]$.

2.2. Trapezoidal model

The trapezoidal cohesive model is characterized by the presence of a *plateau* and the evolution of cohesive interaction is given as follows:

$$T(\Delta_n) = \begin{cases} \sigma_{max}\frac{\Delta_n}{\lambda_1\delta_f}, & \Delta_n < \lambda_1\delta_f, \quad (2a) \\ \sigma_{max}, & \lambda_1\delta_f \leqslant \Delta_n < \lambda_2\delta_f, \quad (2b) \\ \sigma_{max}\frac{\delta_f-\Delta_n}{\delta_f(1-\lambda_2)}, & \lambda_2\delta_f \leqslant \Delta_n < \delta_f, \quad (2c) \\ 0, & \Delta_n \geqslant \delta_f, \quad (2d) \end{cases}$$

where the parameters λ_1 and λ_2 dictate the extension and position of the plateau, while all the other parameters have already been defined in the previous section. In this case, there are four independent cohesive parameters that fully define the cohesive interaction: $\mathbf{X}^T = [\phi_n, \sigma_{max}, \lambda_1, \lambda_2]$.

2.3. Potential-based model

The PPR potential represents the distribution of fracture energy in conjunction with separation of fracture surfaces. The traction separation model is obtained from the first derivative of the potential with respect to the normal opening displacement and, neglecting mixed mode effects, is given by:

[2] The material is no longer able to sustain any load beyond this displacement level.

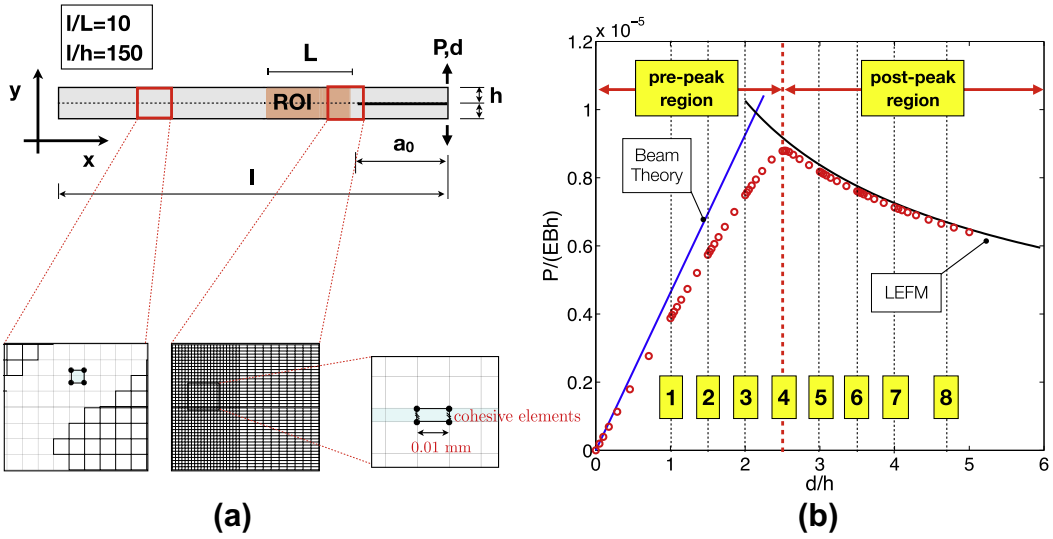

Fig. 2. (a) Schematic of the DCB sample showing details of the finite element mesh. (b) Typical pseudo-experimental global response of the DCB obtained in the forward analysis showing the loading steps at which displacement data are sampled within the ROI. $m = 8$ measurement instants have been employed in the present analysis. Points 1 to 4 are taken in the pre-peak region, while 5 to 8 are taken in the post-peak region. Cohesive elements employed in the forward problem to generate the global response shown here embed the PPR potential based traction–separation relation.

$$T(\Delta_n) = \begin{cases} \frac{\phi_n}{\delta_n}\left(\frac{\alpha}{m}\right)^m \left(1-\frac{\Delta_n}{\delta_n}\right)^{\alpha-1}\left(\frac{m}{\alpha}+\frac{\Delta_n}{\delta_n}\right)^{m-1}(\alpha+m)\frac{\Delta_n}{\delta_n}, & \Delta_n \leqslant \delta_f, \quad (3a) \\ 0, & \Delta_n > \delta_f, \quad (3b) \end{cases}$$

where Δ_n is the opening displacement, ϕ_n is the mode I fracture energy, α is a parameter which controls the shape of the model (see Fig. 1) and δ_n is the final crack opening width:

$$\delta_n = \frac{\phi_n}{\sigma_{max}}\alpha\lambda_n(1-\lambda_n)^{\alpha-1}\left(\frac{\alpha}{m}+1\right)\left(\frac{\alpha}{m}\lambda_n+1\right)^{m-1}, \quad (4)$$

where λ_n is the slope indicator and σ_{max} is the cohesive strength, and m the non-dimensional exponent:

$$m = \frac{\alpha(\alpha-1)\lambda_n^2}{(1-\alpha\lambda_n^2)}. \quad (5)$$

Therefore there are four independent cohesive parameters which need to be determined in order to fully define the cohesive interaction, i.e. $\mathbf{X}^T = [\phi_n, \sigma_{max}, \alpha, \lambda_n]$.

3. Finite element model

The sensitivity analysis has been developed considering a model Double Cantilever Beam made up of steel substrates bonded with an epoxy adhesive. A schematic depiction of the sample is given in Fig. 2. Finite element simulations of debonding were carried out using ABAQUS/Standard and a model of the DCB was prepared assuming that (i) the material behavior outside the cohesive zone is dominated by linear elasticity, and that (ii) the cohesive zone is localized on the crack surfaces. Sample substrates were modeled using four-node continuum elements and assuming plane-stress conditions. It is then assumed that the in-plane surface displacement field can represent the in-plane displacement through the material depth.

The whole adhesive layer was replaced by a single row of cohesive elements with a finite thickness equal to the nominal adhesive layer thickness.[3] Similarly to previous related works (Alfano et al., 2011; Yang et al., 1999; Yang et al., 2001; Yang and Thouless, 2001; Sun et al., 2008), it is then assumed that the role of the adhesive layer is to provide a traction-separation relation across the interface between the two adherents. As a consequence, the macroscopic constitutive behavior of the adhesive is expressed as a function of the opening displacement Δ_n and is captured through the cohesive interaction $T(\Delta_n)$. This simplified modeling enforces constant peel deformation through the thickness of the layer (Yang et al., 1999; Fedele et al., 2009). The area under the traction–separation relation mimics the energy dissipated within the adhesive layer and represents the bond toughness of the joints. The plane model adopted to describe the deformation of the sample was made of 43,000 continuum elements (CPS4), and the adhesive layer was modeled using 1200 cohesive elements. Details concerning the finite element mesh are displayed in Fig. 2. The method was formulated resorting to the principle of virtual work:

$$\left[\int_\Omega \mathbf{B}^T\mathbf{E}\mathbf{B}\,d\Omega - \int_{\Sigma_c}\mathbf{N}_c^T\frac{\partial\mathbf{T}}{\partial\boldsymbol{\Delta}}\mathbf{N}_c\,d\Sigma_c\right]\mathbf{d} = \int_\Sigma \mathbf{N}^T\mathbf{P}\,d\Sigma, \quad (6)$$

where $\mathbf{N}$ and $\mathbf{N}_c$ are matrices of shape functions for bulk and cohesive elements, respectively; $\mathbf{B}$ is the derivative of $\mathbf{N}$; $\mathbf{d}$ are nodal displacements, $\mathbf{E}$ is the material stiffness matrix for the bulk elements, $\frac{\partial\mathbf{T}}{\partial\boldsymbol{\Delta}}$ is the stiffness matrix for cohesive elements and $\mathbf{P}$ is the external traction. The stiffness matrix and load vector of the cohesive elements are assembled in a user-defined subroutine (UEL) within ABAQUS/Standard. An intrinsic[4] CZM implementation was previously employed by the authors to solve non-linear fracture problems and simulate crack propagation (e.g. Alfano et al., 2009). Finally, concerning model boundary conditions, the left hand side of the structure was set free, whereas at the right hand side an increasing opening displacement was applied at the centroid of the upper and lower beams.

[3] The size of cohesive elements was chosen observing that for element sizes $\leqslant$0.1 mm the total dissipated fracture energy (area under the global load–displacement curve) was mesh independent. Therefore, element size was set equal to 0.1 mm throughout the numerical simulations.

[4] In the *intrinsic* implementation of CZM cohesive elements are inserted from the beginning of the analysis along the path of potential crack propagation. In *extrinsic* approaches cohesive elements are inserted once the interface has been predicted to fail based on a selected external criteria.

4. Identification of cohesive models using full-field kinematic data

Previous works have shown that the identification of cohesive model parameters ($\hat{\mathbf{X}}$) based on full field kinematic data is typically carried out by minimizing a proper cost function which quantifies the residual between computed and measured surface displacements across a selected ROI (Shen et al., 2010; Shen and Paulino, 2011; Gain et al., 2011; Fedele et al., 2009; Valoroso and Fedele, 2010; Fedele and Santoro, 2012). Displacement data, which are usually extracted at selected measurement instants during the experiments, are such that they overlap with the finite element model nodal coordinates. Each loading step corresponds to a selected point over the sample load–displacement global response.[5] An objective function $\Phi_2(\mathbf{X}) : \mathbb{R}^p \to \mathbb{R}$, is then minimized through an iterative process, such that:

$$\hat{\mathbf{X}} = \underset{\mathbf{X}\in\mathbb{R}^p}{\arg\min}\{\Phi_2(\mathbf{X})\}, \quad \mathbf{X} \in \Omega_{\mathbf{X}}, \tag{7}$$

where p is the number of input cohesive fracture properties and $\Omega_{\mathbf{X}}$ is the feasible domain for a physically valid cohesive zone model. In the present paper, the data set of the identification process is represented by a time–space sampling of surface displacements concerning a suitable ROI that is monitored during the test. The following cost function has been selected for the sake of the sensitivity analysis:

$$\Phi_2(\mathbf{X}) = \sum_{i=1}^{m} \omega_i(\mathbf{X}) = \sum_{i=1}^{m} \left(\frac{\|u_y^* - u_y(\mathbf{X})\|_2}{max|u_y^*| - |u_y^*|_{ave}} \right)_i, \tag{8}$$

where m are the available measurement instants (i.e. loading steps); u_y^* are the experimentally measured surface displacements; $u_y(\mathbf{X})$ are the corresponding finite element displacement data[6] and $\|\cdot\|$ is the L_2 norm of a vector. For any given measurement instant i, the residuals are normalized by scaling them with the difference between the maximum vertical displacement (in absolute value) and the average displacement within the ROI.[7] The ith residual is based on n_u nodal values and m measurements instants. The contribution of the m residuals are additively included in the scalar function $\Phi_2(\mathbf{X})$. The global load–displacement point data have not been included in $\Phi_2(\mathbf{X})$. As already discussed in previous related works (Alfano et al., 2011, 2009; Valoroso and Fedele, 2010), an identification based on the use of the global response allows the estimation of cohesive energy, but does not provide a reliable identification of other parameters, such as the cohesive strength. For instance, it was shown in Valoroso and Fedele (2010) that including the global response in the objective function does not improve the sensitivity to the initial stiffness of the model.

Since the focus of this work was to effectively perform a global sensitivity analysis, input data were represented by pseudo-experimental displacements generated by means of finite element analyses. Therefore, a *forward* problem was firstly solved, where the cohesive parameters were set equal to arbitrary *true* values ($\tilde{\mathbf{X}}$) and pseudo-experimental displacement maps were generated (i.e., $u_y^* = u_y(\tilde{\mathbf{X}})$). In particular, displacements maps were generated for the selected cohesive models, and using the following input parameters: $\tilde{\mathbf{X}}^{\mathrm{BLN}} = [0.05\,\mathrm{N/mm};\ 20\,\mathrm{MPa};\ 0.1]^T$, $\tilde{\mathbf{X}}^{\mathrm{TPZ}} = [0.05\,\mathrm{N/mm};\ 20\,\mathrm{MPa};\ 0.01;\ 0.5]^T$ and $\tilde{\mathbf{X}}^{\mathrm{PPR}} = [0.05\,\mathrm{N/mm};\ 20\,\mathrm{MPa};\ 6;\ 0.1]^T$. In turn, by varying the input cohesive fracture properties, different values of the objective function were obtained to perform the computation of the sensitivity indexes – which is described in the next section. Notice that the output from each analysis was the displacement field within the ROI at the selected loading steps. Each forward analysis required approximately 100 s on a workstation (2.8 GHz Intel Core i7, 16 Gigabyte RAM). Parameter assignment in FE simulations was made by an automated shell script which generated individual external files with updated cohesive properties which are then recalled by the main job file. Input properties file generation, job submission, data analysis and SA were all made in MATLAB environment.

5. Global sensitivity analysis

Let's consider a mathematical model leading to a deterministic function f, with a set of input data $\mathbf{X}$, such that:

$$f : \mathbb{R}^p \to \mathbb{R}, \tag{9}$$

$$\mathbf{X} \to Y = f(\mathbf{X}). \tag{10}$$

The function f can be very complex and, in practice, is often evaluated through a numerical tool, such as a finite element program. For our current application, vector $\mathbf{X}$ groups all the model's parameters, i.e. the cohesive properties shown earlier, which we assume to be independent. The model output, Y, is supposed to be reduced to one single scalar variable, i.e. the cost function. In order to appreciate the importance of an input variable X_i on Y, one can assess how the variance associated to the model output is reduced when X_i is given a fixed value x_i^*, that is $\mathrm{V}(Y|\mathrm{X}_i = x_i^*)$. The latter represents the *conditional variance* of Y, i.e. the variance on Y taken over all factors excepts X_i. The conditional variance may embed information concerning the sensitivity, since the smaller it is, the greater will be the influence of the variable X_i. However, $\mathrm{V}(Y|\mathrm{X}_i = x_i^*)$ varies with the choice of x_i^*; one can solve this issue by considering the expectation of the conditional variance over the whole domain of definition of the input x_i^*, i.e. $\mathrm{E}[\mathrm{V}(Y|\mathrm{X}_i = x_i^*)]$. However, invoking the *theorem of the total variance* (Saltelli et al., 2008), which reads:

$$\mathrm{V} = \mathrm{V}(Y) = \mathrm{E}[\mathrm{V}(Y|\mathrm{X}_i)] + \mathrm{V}[\mathrm{E}(Y|\mathrm{X}_i)], \tag{11}$$

(where x_i^* has been dropped for conciseness), we can use as an indication of the sensitivity of Y to X_i the variance of the expectation of Y conditional to X_i. The more relevant the effect of X_i is, the more the previous quantity will increase. We can now define the first order Sobol sensitivity index of Y to X_i as follows:

$$S_i = \frac{\mathrm{V}_i}{\mathrm{V}} = \frac{\mathrm{V}(\mathrm{E}[Y|\mathrm{X}_i])}{\mathrm{V}}, \tag{12}$$

that is always between 0 and 1, and the bigger it is the higher will be the influence of X_i. Computation of sensitivity indexes has been performed using Sobol decomposition, Monte Carlo integrals and quasi random sampling; further details concerning the computational procedure are given in the appendices.

6. Results and discussion

The global response of the DCB sample, obtained running a forward analysis, is shown in Fig. 2. Analytical solutions for pre-peak and post-peak regions, stemming from beam theory and linear elastic fracture mechanics, are also superimposed (Alfano et al.,

[5] Notice that loading steps are usually selected from post-peak region; global response curve is not always employed in the inverse identification (i.e. is not included in the cost function) (Shen et al., 2010; Shen and Paulino, 2011; Gain et al., 2011).

[6] Additional simulations, not reported herein for brevity, have shown that adding surface displacement in the x-direction does not modify the results quoted in the paper.

[7] In a preliminary stage we assessed different objective functions by essentially using different norms (e.g. L_1 and L_2) as well as different scaling quantities to get non-dimensional residuals. Specifically, ϕ_n and σ_{max} were varied in ranges centered around a set of *true* cohesive properties, i.e. input properties employed to generate *synthetic* experimental data. Therefore, several values of the objective function were obtained. Surface plots of these data have shown that the selected objective function is "sharper" around the minimum value.

2011). Notice that fracture energy controls the descending part of the load–deflection curve of the DCB while the initial slope is mostly dictated by cohesive stress (Alfano et al., 2009). It is then expected that the sensitivity of Φ_2 to cohesive fracture properties will be affected not only by displacement sampling in space, i.e. size of the region of interest (ROI), but also by sampling in time, i.e. the selected loading steps used as input. The influence of both parameters will be therefore investigated. The m loading steps at which surface displacements maps are extracted from FE analyses to build-up pseudo experimental data are also shown in Fig. 2. These are evenly distributed in the two above mentioned regions. Concerning the selection of the ROI size, the main physical requirement is that it needs to embed the fracture process zone (FPZ) behind the advancing crack tip at the m loading steps included in the objective function. It is in this region that the displacement field is expected to be sensitive to the details of the traction distribution within the cohesive zone. For the present work we found that a maximum size of the ROI (L) equal to 1/10 the overall length (l) of the sample provided satisfactory results (see Fig. 2) since the FPZ was always inside the region of interest in all the selected loading steps. Notice that the ROI size could vary *lengthwise* as schematically shown in Fig. 3. In particular, an abscissa x^* was defined such that the size of the ROI could range from its maximum length L, when $x^* = 0$, to L–L_1, when $x^* = L_1$. Length L_1 is an arbitrarily selected parameter which has been chosen such that at least 1/8 of the maximum size of the ROI is included in the objective function. It is worth noting that the size of the FPZ depends on the specific material properties of the sample, i.e. stiffness of the substrates, and the adopted cohesive properties. In other words, different combinations of cohesive properties (i.e. different material systems in actual experiments) may require the use of ROI with different (maximum) size, which therefore should be chosen according to the problem at hand. In principle, even the whole sample surface could be employed from a technical viewpoint, and this is something that has been done in previous works (Shen et al., 2010; Shen and Paulino, 2011; Gain et al., 2011). While this strategy would certainly require a much higher computational effort, advantages in term of sensitivity are not guaranteed. Indeed, it might be possible that large areas far away from the FPZ are included in the objective function. These areas contribute to the computational expenditure (e.g. storage and manipulation of large arrays of displacement data) but do not necessarily carry over useful information for the identification process.

As a result the pseudo-experimental kinematic data u_y^* have been assembled in a $(n_u \times m)$-dimensional matrix containing the n_u nodal displacements within the ROI for each measurement instant i ($i = 1,\ldots,m$) which have been additively included in the cost function $\Phi_2(\mathbf{X})$. In the present work the overall (maximum) number of input displacements in the ROI is equal to around 35,000 while $m = 8$ measurement instants have been considered. In order to assess the effect of data sampling, both figures have been varied in the sensitivity analysis. Specifically, the effect of time sampling has been studied by performing the sensitivity analysis for different combinations of loading steps. In a similar manner, the effect of space sampling (i.e. the number of nodal displacements included in the ROI) has been analyzed by progressively decreasing its length as illustrated in Fig. 3 and discussed earlier in this section.

6.1. Graphical representation through scatter plots

A visualization of the sensitivity of the model output to changes in cohesive zone properties can enhance results interpretation. The results can indeed be represented graphically through *scatter plots*. These last are obtained by performing model evaluations for the quasi random sequence of N parameters sets ($\mathbf{X}$) and projecting the results on a specific plane to yield a cloud of points. A sample size of $N = 750$ was used to assess the first order sensitivity effect of the p input parameters associated to the selected cohesive models. Analyses carried out with samples of higher dimensions ($N = 1500$) have shown results essentially similar to that reported later in the paper. Therefore, p graphs of one-dimensional slices of the response surface are constructed, each representing the global sensitivity of the model to a specific parameter. Notice that the

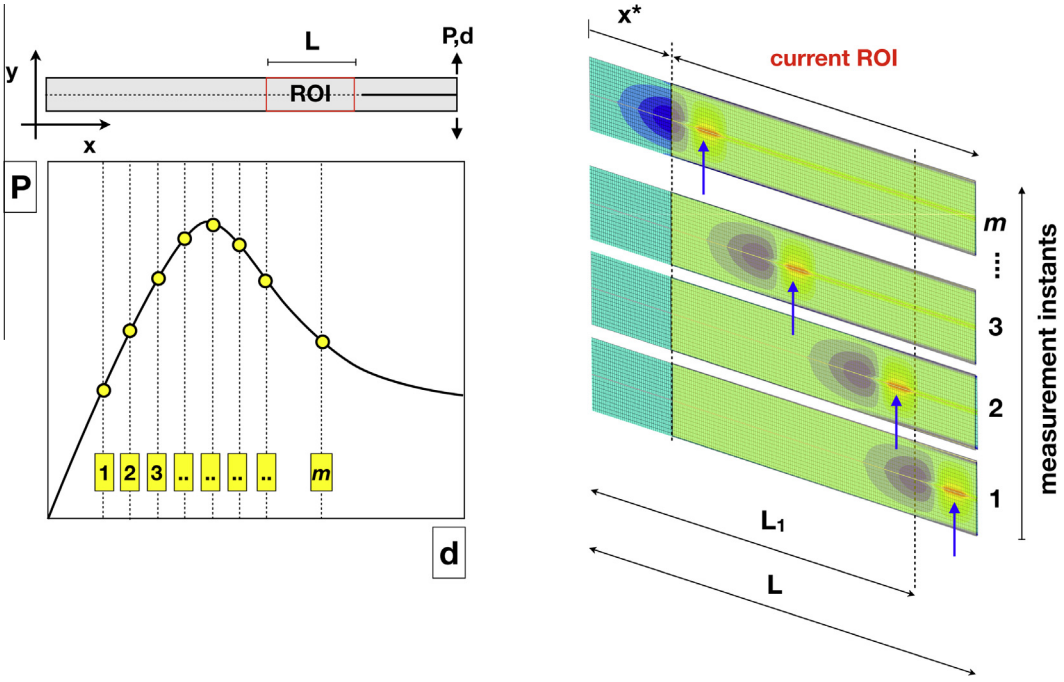

Fig. 3. Region of interest selected to extract surface displacements at m measurement instants; the current size of the ROI is determined by the abscissa x^* ($0 \leqslant x^* \leqslant L_1$) such that its extension in the x-direction ranges from L–L_1 for $x^* = L_1$ to L for $x^* = 0$. The arrows point to the approximate location of the fracture process zone.

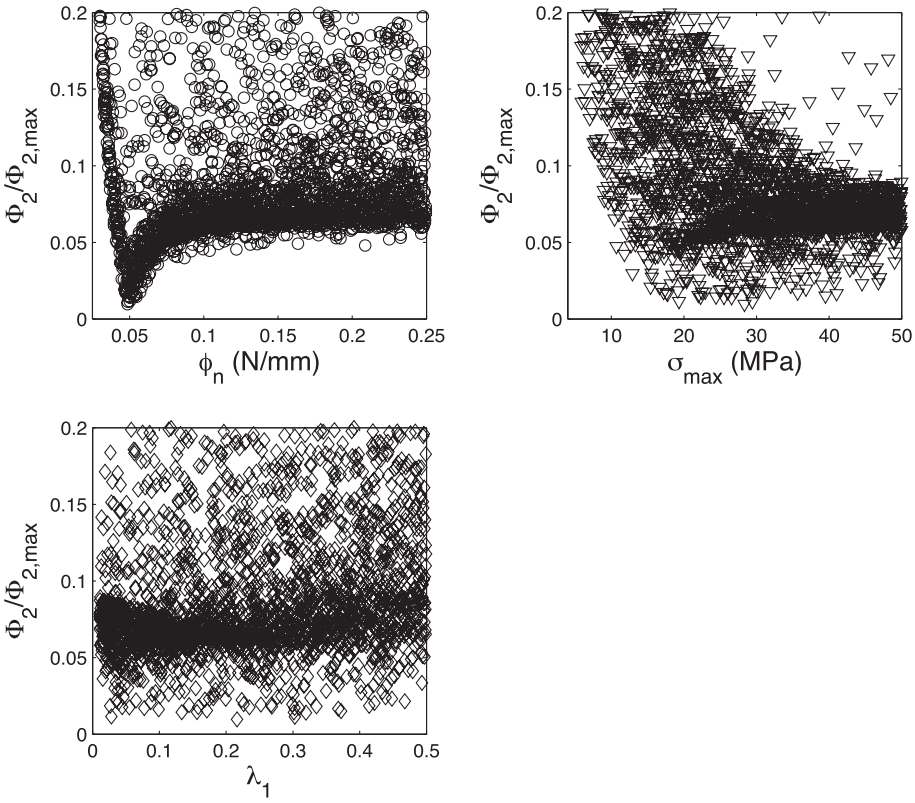

Fig. 4. Scatter plots obtained using the bilinear model (BLN). The objective function includes the full set of displacement data extracted at measurement instants 1 to 8. Input cohesive fracture properties for generating pseudo-experimental data were: $\mathbf{X}$ = [0.05 N/mm; 20 MPa; 0.1]. The effect of ϕ_n and σ_{max} is apparent since the data is aggregated around the input values employed to generate synthetic data. The effect of λ_1 seems to be negligible.

points in the scatter plots are always the same though sorted differently. This graphical representation can quickly reveal the marginal influence of one or more parameters on the model output. Indeed, if the points are randomly spread over the parameter range, this can indicate that the parameter does not influence the model output. On the contrary, if a pattern is observed in the scatter plot, in turn the parameter influences the model output to some extent.

The scatter plots pertaining to the analyzed cohesive models are reported in Figs. 4–6. In all cases, the full size of the ROI and $m = 8$ number of loading steps have been considered. The results, clearly show that for the problem addressed herein, parameters which control the initial stiffness and the shape of the model (i.e. λ_1, λ_2, α and λ_n) do not sensitively affect the displacement field and, in turn, the objective function.[8] On the other hand, displacement field in the ROI looks to be mostly sensitive to cohesive energy and cohesive strength. The data points are indeed always distributed around the input cohesive properties employed to generate the pseudo experimental displacement maps, i.e. $\phi_n = 0.05$ N/mm and $\sigma_{max} = 20$ MPa. These results suggest that, for the given set of experimental data (surface displacements), cohesive parameters other than energy and strength can be hardly determined.

Given the similarity of the obtained results among the different cohesive models, in the remainder of the paper only the results pertaining to the PPR model will be presented and discussed. In order to highlight the effect of time sampling, two additional scatter plots have been generated considering a reduced number of loading steps. In particular, Fig. 7 shows the scatter plots for the PPR model when feeding the objective function Φ_2 with loading steps 1 to 4 (pre-peak region). It is apparent, that *eliminating data from the post-peak region*, greatly affect the sensitivity to ϕ_n, since the data distribution is now pretty uniform over the whole range of this parameter. On the other hand, the sensitivity to σ_{max} seems to be improved since the shape of the corresponding plot is such that the data is more distributed around the input value of σ_{max} employed to generate synthetic data. Fig. 8 now shows the opposite case, i.e. *eliminating data from the pre-peak region of global response*. As expected, the data points in the ϕ_n plot are now shaped so that the peak occurs around the input cohesive energy. However, the sensitivity to σ_{max} seems to be lost since the data is evenly spread over the whole parameter range. These results stress the importance of data sampling in time.

6.2. Effect of displacement sampling in time and space

As mentioned earlier, the basic outcome of the present Sobol SA are the first order sensitivity indexes associated to the cohesive fracture properties, i.e. S_i. The variation of sensitivity to displacement sampling in time and space is now assessed on quantitative ground through the analysis of the obtained S_i. The variation of S_i for different choices of time sampling is shown in Fig. 9. In particular, the objective function is progressively fed with a decreasing number of loading steps from the post-peak region. Accordingly, the sensitivity to cohesive stress increases while that to cohesive energy decreases and becomes negligible when the loading steps from the post-peak region are no longer included in the cost function. Notice that S_α and S_{λ_n} are always very low, and this was somewhat expected based on the observation of the scatter plots presented in the previous section. In a similar fashion, by including more steps from the post peak region it introduces a greater sensitivity to cohesive energy rather than cohesive strength. This is

[8] The Y data is uniformly distributed over the slices, therefore this is not an important factor.

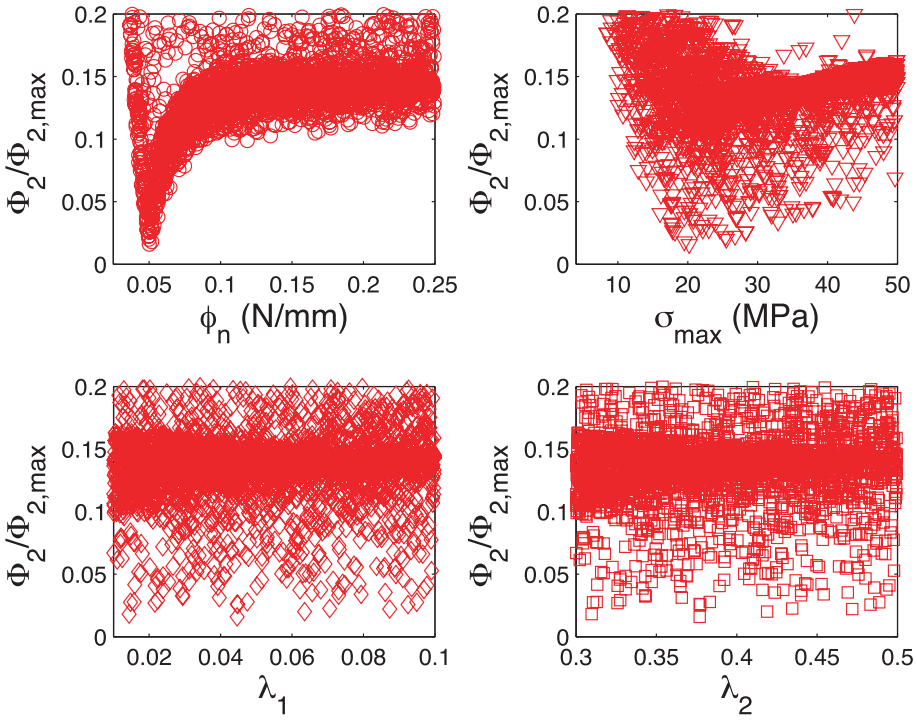

Fig. 5. Scatter plots obtained using the trapezoidal model (TPZ). The objective function include the full set of displacement data extracted at measurement instants 1 to 8. Input cohesive fracture properties for generating pseudo-experimental data were: $\bar{\mathbf{X}}$ = [0.05 N/mm; 20 MPa; 0.01; 0.5]. The effect of ϕ_n and σ_{max} is apparent since the data is aggregated around the input values employed to generate synthetic data while λ_1 and λ_2 seems to be of secondary importance.

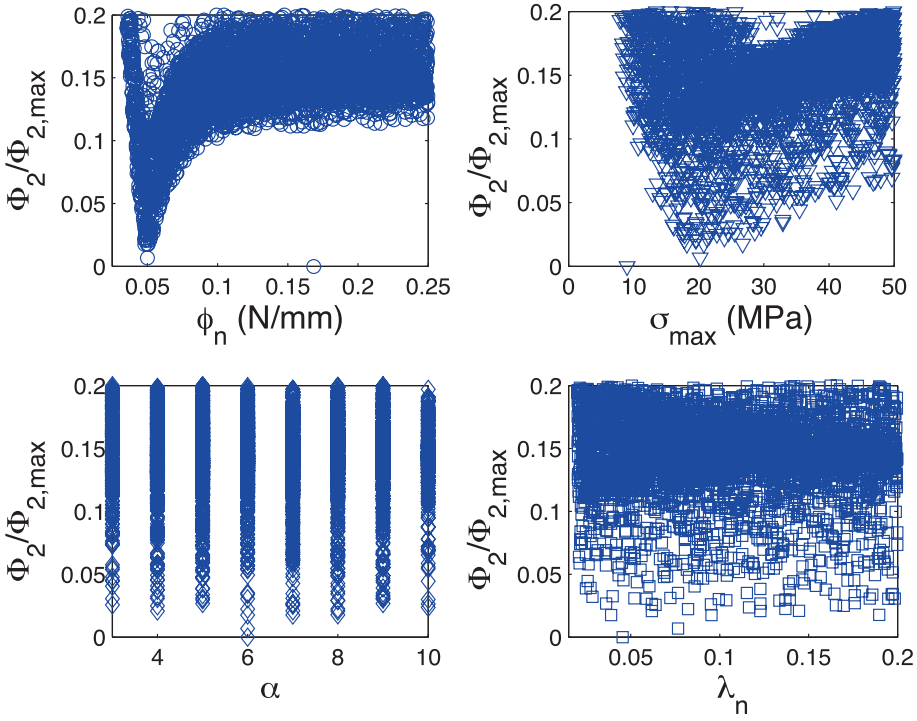

Fig. 6. Scatter plots obtained using the PPR model. The objective function include the full set of displacement data extracted at measurement instants 1 to 8. Input cohesive fracture properties for generating pseudo-experimental data were: $\bar{\mathbf{X}}$ = [0.05 N/mm; 20 MPa; 6; 0.1]. The effect of ϕ_n and σ_{max} is apparent since the data is aggregated around the input values employed to generate synthetic data while α and λ_n seems to be of secondary importance.

illustrated by Fig. 10 where the objective function is fed with an increasing number of loading steps from the post-peak region. It is apparent that the sensitivity to cohesive energy is improved, although that to cohesive stress decreases. On the basis of these results, in principle, it could be possible to *tailor* the content of the objective function so that to balance the sensitivity to cohesive energy and cohesive strength. This is shown by the bar diagrams of Fig. 11. By properly combining intermediate loading steps (from 2 to 6) a nearly equal sensitivity to ϕ_n and σ_{max} is achieved. We finally discuss the effect of displacement sampling in space. To this

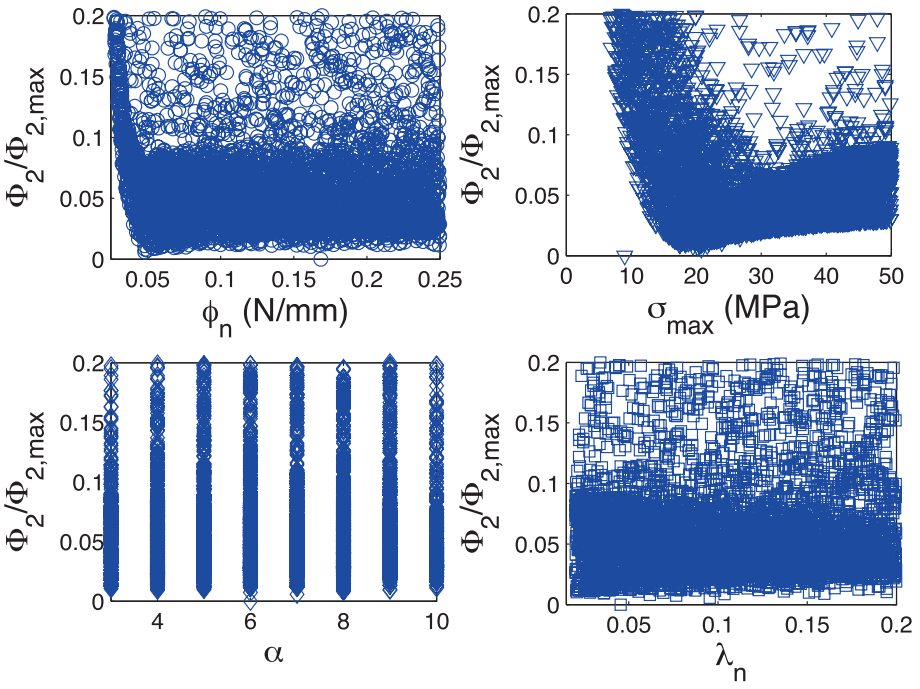

Fig. 7. Scatter plots obtained using the PPR model. The objective function include the full set of displacement data extracted at measurement instants 1 to 4. The sensitivity to cohesive energy decreases because the data in the scatter plot pertaining to cohesive energy have uniform distribution over the whole range. On the other hand the sensitivity to cohesive stress improved. Sensitivity to the other parameters remains low.

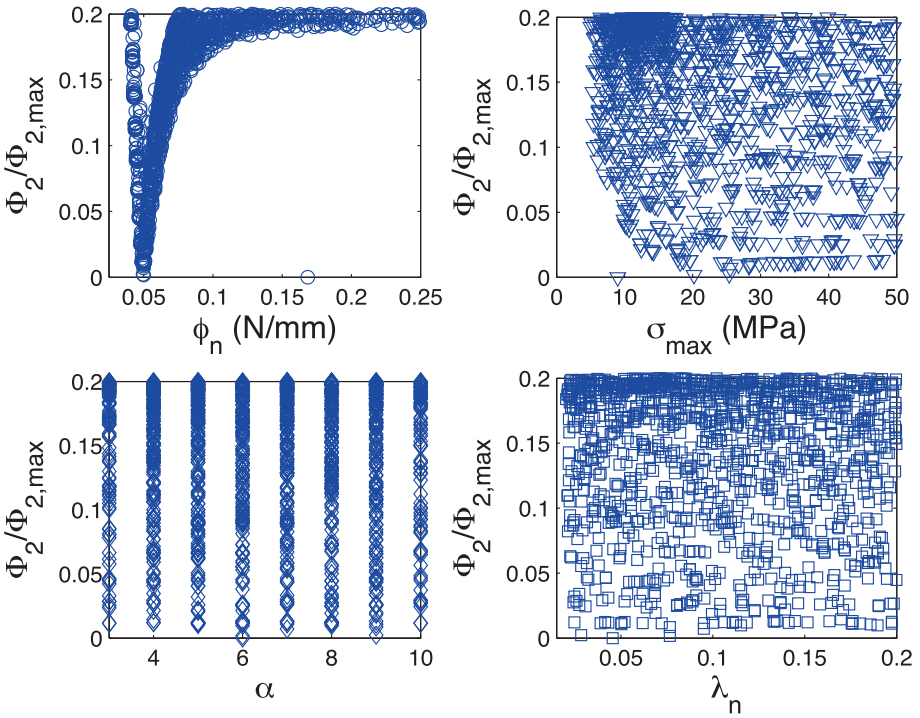

Fig. 8. Scatter plots obtained using the PPR model. The objective function include the full set of displacement data extracted at measurement instants 4 to 8. The sensitivity to cohesive stress decreases because the data in the scatter plot pertaining to cohesive stress have uniform distribution over the whole range. On the other hand the sensitivity to cohesive energy improved. Sensitivity to the other parameters remains low.

purpose, ROI size has been progressively reduced lengthwise, as already explained earlier in the paper, and the sensitivity indexes have been computed for each updated size of the ROI. The results are shown in Fig. 12. For a given number of input loading steps, a smaller ROI enhances the sensitivity to cohesive stress, but decreases that to cohesive energy.

6.3. Discussion

The global sensitivity analysis (SA) can help to ascertain which are the most influential parameters of a model to determine which of them should be incorporated in the identification process. The results of the SA have shown that surface displacements in the

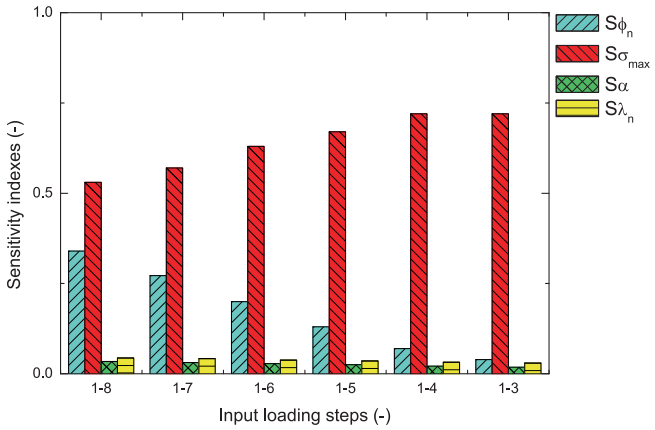

Fig. 9. Bar diagrams showing the evolution of the sensitivity indexes for a decreasing number of loading steps included in the objective function. Notice that loading steps from the post-peak region are progressively reduced. Accordingly the sensitivity to cohesive energy is reduced.

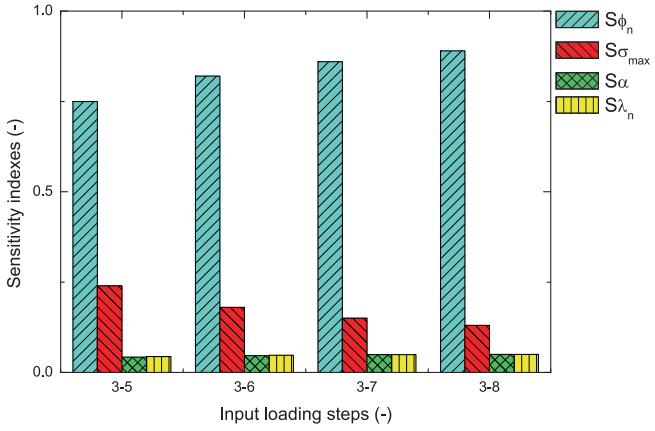

Fig. 10. Bar diagrams showing the evolution of the sensitivity indexes for an increasing number of loading steps included in the objective function. Notice that the inclusion of loading steps from the post-peak region progressively enhances the sensitivity to cohesive energy.

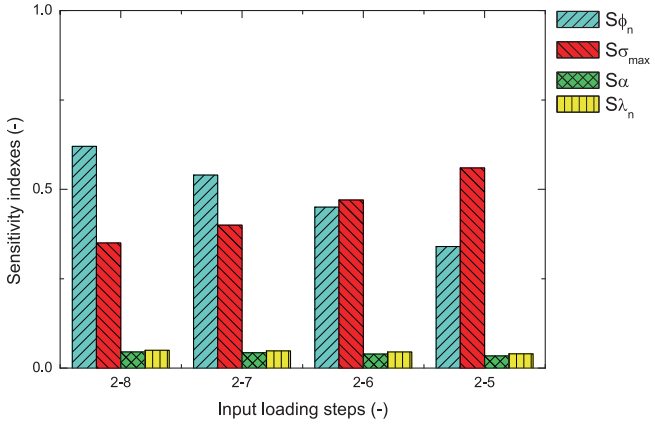

Fig. 11. Bar diagrams illustrating a potential tailoring of the data set to be included in the cost function in order to balance the sensitivity to cohesive energy and cohesive stress. For the problem analyzed herein, it is apparent that combining kinematic from the intermediate steps can lead to nearly equal sensitivity to cohesive energy and cohesive strength.

DCB model are primarily dependent on cohesive energy and cohesive strength, while the effect of model shape appears to be not significant on the outcome of the model. It is then concluded that the full set of cohesive properties is not always obtainable from the available kinematic data. As a consequence, it is not needed to include all model parameters to obtain an efficient identification. Moreover, displacement sampling in time and space have been found to have a different impact on the estimation of ϕ_n and σ_{max}. Their identification may be not equally accurate and robust depending on the amount of data included in the objective function. In particular, the obtained results suggest that alternative identification strategies could be devised on the basis of a proper use of the information provided by a global SA. For example, considering the specific problem addressed in the paper, one could develop a two-step identification approach where the post-peak steps are employed to identify cohesive energy, and subsequently use the pre-peak steps only to identify cohesive strength.

It is worth emphasizing that the low sensitivity to parameters related to the shape of the model may be related to the specific problem analyzed herein, that is the analysis of a DCB sample made up of stiff substrates bonded with an adhesive (i.e. a classical adhesive joint design). Although representative of a multitude of practical material systems, this choice does not promote the sensitivity to the details of the traction profile across the interface. Cohesive zone size should be first of all relatively large, so that there is more substrate material near the cohesive zone to be directly affected. However, if the ratio of cohesive strength to bulk elastic modulus is not large enough, the displacement field can be smeared by the rigidity of the substrate. This limitation is directly related to the resolution of the displacement field, indeed higher displacement resolution would allow the identification of the full set of properties, even for shorter cohesive zone and lower cohesive traction.

7. Concluding remarks

In this paper a global (Sobol) sensitivity analysis in the identification of the cohesive zone model using full-field kinematic data was made for the first time. The Sobol analysis technique is based on variance decomposition and is able to handle non-linear and non-monotonic models. In general, the results have shown that the use of Sobol analysis can highlight which parameters can be determined with the available experimental data. As a result, the so obtained sensitivity indexes can be effectively used for both factor fixing and factor prioritization in view of the identification process. The graphical representations by means of scatter plots gave meaningful insights on the influence of the input parameters on the model output. Clear trends were observed for (highly) influential parameters, such as cohesive energy and cohesive strength, which appeared to have the most important first order effect on the cost function. Moreover, the approach proposed herein, which makes use of FE simulations driven by a MATLAB script, is quite flexible and, as such, is prone to generalizations to different geometries and loading conditions (i.e. mixed mode), and can include nonlinearities in the bulk material with minor modifications. From this standpoint, the use of a similar framework for the identification of mode II and mixed mode cohesive models is certainly possible. However, in the case of mixed mode fracture, possible interactions among variables must be taken into account by including the computation of second order indexes.

Finally, it is recognized that in real measurements, spatial resolution, noise and other experimental errors, such as out-of-plane displacements and missing data points, strongly influence the identification process. The performed sensitivity analysis aims to study how variations in the displacement field in the monitored

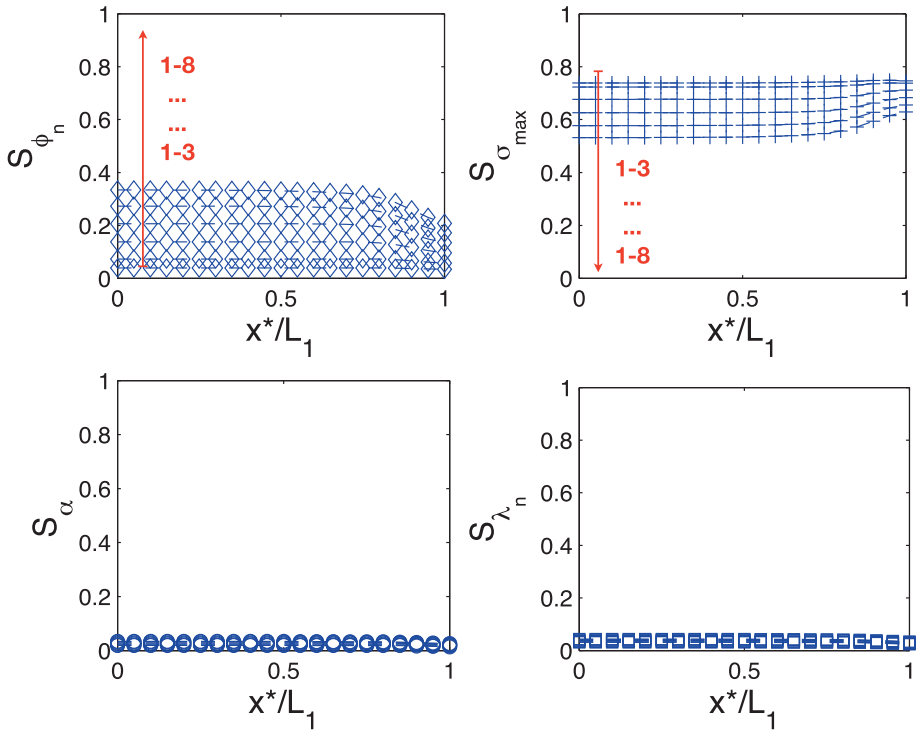

Fig. 12. Distribution of the first order sensitivity indexes for varying dimensions in the x-direction of the ROI. The dimension decreases for increasing values of x^*/L. The arrows pointing upward denote an increase in the number of loading steps included in the objective function. In all the results the input displacement data are alway taken from the pre-peak region and progressively include the subsequent remaining steps.

subdomain (ROI), can be attributed to variations in the input cohesive properties. The sources of error outlined above represent additional (interfering) inputs to which the output is *unintentionally* sensitive. Including these inputs in the sensitivity analysis would be certainly possible (i.e. it would imply the use of an additional variable in the SA). However, this would not change the key conclusions of the paper, i.e. for the problem at hand some parameters of the models cannot be identified using full field data. Future investigations will be devoted to results validation based on use of truly experimental data. From this standpoint, a data selection strategy based on the so obtained sensitivity indexes will be devised since it appears to be the most appropriate basis for data sampling in time and space to be included in the cost function.

Acknowledgements

The authors wish to thank King Abdullah University of Science and Technology (KAUST) for supporting this research. M.A. gratefully acknowledges the financial support from University of Calabria (ex MURST 60%), and the support received from University of Illinois during his visit at the Department of Civil and Environmental Engineering in 2013.

Appendix A. Sobol decomposition

In order to compute the sensitivity indexes, Sobol suggested to decompose the function f into summands of increasing dimensionality. Specifically, assuming that the input variables belong to the interval $[0,1]^p$, the function $f(\mathrm{X}_1,\ldots,\mathrm{X}_p)$ was decomposed as follows:

$$f(\mathrm{X}_1,\ldots,\mathrm{X}_p) = f_0 + \sum_{i=1}^{p} f_i(\mathrm{X}_i) + \sum_{1\leqslant i<j\leqslant p} f_{i,j}(\mathrm{X}_i,\mathrm{X}_j) + \cdots + f_{1,2,\ldots,p}(\mathrm{X}_1,\ldots,\mathrm{X}_p),$$

where f_0 is a constant and the functions of the decomposition verify the conditions:

$$\int_0^1 f_{i_1,\ldots,i_s}(x_{i_1},\ldots,x_{i_s})\,dx_{i_k} = 0, \tag{A.1}$$

$\forall k = 1,\ldots,s$ and $\forall\{i_1,\ldots,i_s\} \in \{1,\ldots,p\}$. The existence and the uniqueness of the solution are guaranteed by conditions (A.1). In this framework, decomposition (A.1) is called the Analysis of Variance (ANOVA) decomposition. The immediate consequence of this decomposition is an orthogonality property; indeed, provided that at least one index is not shared among subsets $[i_1,\ldots,i_s]$ and $[j_1,\ldots,j_t]$, it follows that

$$\int_0^1 f_{i_1,\ldots,i_s}(x_{i_1}\ldots,x_{i_s}) f_{j_1,\ldots,j_t}(x_{j_1}\ldots,x_{j_t})\,dx = 0. \tag{A.2}$$

Then, one can use conditions (A.1) step by step to get by integration over all the variables:

$$\int_0^1 f(x)\,dx = f_0. \tag{A.3}$$

By integration over all the data, except X_i (since $\mathrm{X}_{\sim i}$ is the vector of all the variables except i):

$$\int_0^1 f(x)\,dx_{\sim i} = f_0 + f_i(\mathrm{X}_i), \tag{A.4}$$

by integration over all the variables, except X_i and X_j:

$$\int_0^1 f(x)\,dx_{\sim ij} = f_0 + f_i(\mathrm{X}_i) + f_j(\mathrm{X}_j) + f_{i,j}(\mathrm{X}_i,\mathrm{X}_j), \tag{A.5}$$

and so on. Thus, one gets the elementary functions of the decomposition:

$$f_0 = \int_0^1 f(x)\,dx, \tag{A.6}$$

$$f_i(X_i) = \int_0^1 f(x)dx_{\sim i} - f_0, \tag{A.7}$$

$$f_{ij}(X_i, X_j) = \int_0^1 f(x)dx_{\sim ij} - f_0 - f_i(X_i) - f_j(X_j), \tag{A.8}$$

etc. The previous decomposition can be interpreted using the common terminology of expectation and variance, and the equations can be rewritten as follows:

$$f_0 = E[Y], \tag{A.9}$$

$$f_i(X_i) = E[Y|X_i] - E[Y], \tag{A.10}$$

$$f_{ij}(X_i, X_j) = E[Y|X_i, X_j] - E[Y|X_i] - E[Y|X_j] + E[Y]. \tag{A.11}$$

It is relatively straightforward to prove that the variance of function Y can also be divided according to the ANOVA decomposition. The variance of the model (under the assumption that the data are independent) can be divided into:

$$V = \sum_{i=1}^{p} V_i + \sum_{1 \leqslant i < j \leqslant p} V_{ij} + \cdots + V_{1\ldots p}, \tag{A.12}$$

where

$$V_i = V(E[Y|V_i]), \tag{A.13}$$

$$V_{ij} = V(E[Y|V_i, V_j]) - V_i - V_j, \tag{A.14}$$

$$V_{ijk} = V(E[Y|V_i, V_j, V_k]) - V_{ij} - V_{ik} - V_{jk} - V_i - V_j - V_k. \tag{A.15}$$

Using that decomposition, the first-order sensitivity indices (S_i) can be obtained as shown in Section 5, while the second-order sensitivity indices are:

$$S_{ij} = \frac{V_{ij}}{V}, \tag{A.16}$$

which represents the sensitivity of the variance of Y due to the interaction between the variables X_i and X_j. When these sensitivity indexes are calculated theoretically, they verify the following properties: (1) they are all positive (2) their sum is equal to 1 (3) the influence of the associated variable increases as the value of the Sobol index approaches 1.

Appendix B. Monte Carlo integrals and Sobol quasi-random sampling

Sensitivity indexes can be determined provided the function f is known analytically and it is relatively simple. However, for the problem considered herein, the cost function may be quite complex and highly non-linear and its analytical equation is not known. In this case, the sensitivity indexes are estimated using Monte Carlo integrals. Indeed, deterministic numerical integration algorithms work well provided the number of dimensions in the problem is small. For increasing number of dimensions, function evaluations increase quickly. Monte Carlo methods are useful in such cases, and allow to estimate the integrals by randomly selecting N points over the p-dimensional space[9]. Let consider a N-dimensional sample of the input parameters of the model, i.e. $(X_1, \ldots, X_p)$, such that

$$\widetilde{X}_{(N)} = (x_{k1}, x_{k2}, \ldots, x_{kp})_{k=1\ldots N}, \tag{B.1}$$

the expectation of Y, $E[Y] = f_0$, and the variance, $V(Y)$ can be estimated using Monte Carlo integrals such that:

$$\hat{f}_0 = \frac{1}{N}\sum_{k=1}^{N} f(x_{k1}, x_{k2}, \ldots, x_{kp}), \tag{B.2}$$

$$\hat{V} = \frac{1}{N}\sum_{k=1}^{N} f^2(x_{k1}, x_{k2}, \ldots, x_{kp}) - \hat{f}_0^2. \tag{B.3}$$

Sobol proposed to estimate the first order sensitivity index as follows:

$$S_i = \frac{\hat{V}_i}{\hat{V}} = \frac{\hat{U}_i - \hat{f}_0^2}{\hat{V}}, \tag{B.4}$$

where $\hat{U}_i$ is estimated as a classical expectancy:

$$\hat{U}_i = \frac{1}{N}\sum_{k=1}^{N} f\left(x_{k1}^{(1)}, \ldots, x_{k(i-1)}^{(1)}, x_{ki}, x_{k(i+1)}^{(1)} \ldots, x_{kp}^{(1)}\right) \times f\left(x_{k1}^{(2)}, \ldots, x_{k(i-1)}^{(2)}, x_{ki}, x_{k(i+1)}^{(2)} \ldots, x_{kp}^{(2)}\right) \tag{B.5}$$

but keeping x_{ki} fixed within the two calls to the function f. Monte Carlo methods featuring random sampling is the basic route to compute Monte Carlo integrals. However, a wide range of alternative sampling techniques are available to increase the convergence rate. In this paper, a quasi random sequence (namely Sobol sequence) has been employed. These sequences make use of a base of two to form successively fine uniform partitions of the unit interval. Finally, coordinates in each dimension are reordered. By using pseudo-random sampling, the convergence rate is faster than other methods (Saltelli et al., 2008).

[9] Given the Theorem of the Central Limit, this method displays $1/\sqrt{N}$ convergence rate.

References

Abanto-Bueno, J., Lambros, J., 2005. Experimental determination of cohesive failure properties of a photodegradable copolymer. Exp. Mech. 45 (2), 144–152.

Adams, R.D., Comyn, J., Wake, W.C., 1997. Structural Adhesives Joints in Engineering. Chapman and Hall.

Alfano, M., Furgiuele, F., Leonardi, A., Maletta, C., Paulino, G.H., 2009. Mode I fracture of adhesive joints using tailored cohesive zone models. Int. J. Fract. 157, 193–204.

Alfano, M., Furgiuele, F., Lubineau, G., Paulino, G.H., 2011. Simulation of debonding in Al/epoxy T-peel joints using a potential based cohesive zone model. Procedia Eng. 10, 1760–1765.

Alfano, M., Lubineau, G., Furgiuele, F., Paulino, G.H., 2011. On the enhancement of bond toughness for Al/epoxy T-peel joints with laser treated substrates. Int. J. Fract. 171, 139–150.

Alfano, M., Furgiuele, F., Pagnotta, L., Paulino, G.H., 2011. Analysis of fracture in aluminum joints bonded with a bi-component epoxy adhesive. J. Test. Eval. 39 (2) (JTE102753).

Avril, S., Bonnet, M., Bretelle, A.-S., Grédiac, M., Hild, F., Ienny, P., Latourte, F., Lemosse, D., Pagano, S., Pagnacco, E., Pierron, F., 2008. Overview of identification methods of mechanical parameters based on full-field measurements. Exp. Mech. 48 (4), 381–402.

Barenblatt, G.I., 1962. Mathematical theory of equilibrium cracks in brittle fracture. Adv. Appl. Mech. 7, 55–129.

Blaysat, B., Florentin, E., Lubineau, G., Moussawi, A., 2012. A Dissipation Gap Method for full-field measurement-based identification of elasto-plastic material parameters. Int. J. Numer. Methods Eng. 91 (7), 685–704.

Cavalli, M.N., Thouless, M.D., 2001. The effect of damage nucleation on the toughness of an adhesive joint. J. Adhes. 76 (1), 75–92.

Dugdale, D.S., 1960. Yielding steel sheets containing slits. J. Mech. Phys. Solids 8 (2), 100–104.

Fedele, R., Santoro, R., 2012. Extended identification of mechanical parameters and boundary conditions by digital image correlation. Procedia IUTAM 4, 40–47.

Fedele, R., Raka, B., Hild, F., Roux, S., 2009. Identification of adhesive properties in GLARE assemblies using digital image correlation. J. Mech. Phys. Solids 57, 1003–1016.

Florentin, E., Lubineau, G., 2010. Identification of the parameters of an elastic material model using the constitutive equation gap method. Comput. Mech. 46 (4), 521–531.

Gain, A.L., Carroll, J., Paulino, G.H., Lambros, J., 2011. A hybrid experimental/numerical technique to extract cohesive fracture properties for mode-I fracture of quasi-brittle materials. Int. J. Fract. 169, 113–131.

Gowrishankar, S., Mei, H., Liechti, K.M., Huang, R., 2012. A comparison of direct and iterative methods for determining traction-separation relations. Int. J. Fract. 177 (2), 109–128.

Kinloch, A.J., 1987. Adhesion and Adhesives, Science and Technology. Chapman and Hall.

Lee, M.J., Cho, T.M., Kim, W.S., Lee, B.C., Lee, J.J., 2010. Determination of cohesive parameters for a mixed mode cohesive zone model. Int. J. Adhes. Adhes. 30, 322–328.

Lubineau, G., 2009. A goal-oriented field measurement filtering technique for the identification of material model parameters. Comput. Mech. 44 (5), 591–603.

Moussawi, A., Lubineau, G., Florentin, E., Blaysat, B., 2013. The constitutive compatibility method for identification of material parameters based on full-field measurements. Comput. Method Appl. Mech. 265, 1–14.
Park, K., Paulino, G.H., 2013. Cohesive Zone models: a critical review of traction-separation relationships across fracture Surfaces. Appl. Mech. Rev. 64 (6) (Art. no. 060802).
Park, K., Paulino, G.H., Roesler, J.R., 2009. A unified potential-based cohesive model of mixed-mode fracture. J. Mech. Phys. Solids 57, 891–908.
Pottier, T., Toussaint, F., Vacher, P., 2011. Contribution of heterogeneous strain field measurements and boundary conditions modelling in inverse identification of material parameters. Eur. J. Mech. A-Solids 30 (3), 373–382.
Saltelli, A., Ratto, M., Andres, T., Campolongo, F., Cariboni, J., Gatelli, D., Saisana, M., Tarantola, S., 2008. Global Sensitivity Analysis: The Primer. Wiley.
Shen, B., Paulino, G.H., 2011. Direct extraction of cohesive fracture properties from digital image correlation: a hybrid inverse technique. Exp. Mech. 51 (2), 143–161.
Shen, B., Stanciulescu, I., Paulino, G.H., 2010. Inverse computation of cohesive fracture properties from displacement fields. Inverse Prob. Sci. Eng. 18 (8), 1103–1128.
Sridharan, S., 2008. Delamination Behavior of Composites. CRC-WP.
Sun, C., Thouless, M.D., Waas, A.M., Schroeder, J.A., Zavattieri, P.D., 2008. Ductile-brittle transition in the fracture of plastically deforming adhesively bonded structures. Part II: Numerical studies. Int. J. Solids Struct. 45, 4725–4738.
Sutton, M.A., Orteu, J.-J., Schreier, H.W., 2009. Image Correlation for Shape, Motion and Deformation Measurements. Springer.
Tan, H., Liu, C., Huang, Y., Geubelle, P., 2006. The cohesive law for the particle/matrix interfaces in high explosives. J. Mech. Phys. Solids 53 (8), 1892–1917.
Valoroso, N., Fedele, R., 2010. Characterization of a cohesive-zone model describing damage and de-cohesion at bonded interfaces. Sensitivity analysis and mode-I parameter identification. Int. J. Solids Struct. 47 (13), 1666–1677.
van den Bosch, M.J., Schreurs, P.J.G., Geers, M.G.D., 2008. Identification and characterization of delamination in polymer coated metal sheet. J. Mech. Phys. Solids 56, 3259–3276.
Yang, Q.D., Thouless, M.D., 2001. Mixed mode fracture analyses of plastically deforming adhesive joints. Int. J. Fract. 110, 175–187.
Yang, Q.D., Thouless, M.D., Ward, S.M., 1999. Numerical simulations of adhesively bonded beams failing with extensive plastic deformation. J. Mech. Phys. Solids 47, 1337–1353.
Yang, Q.D., Thouless, M.D., Ward, S.M., 2001. Elastic–plastic mode-II fracture of adhesive joints. Int. J. Solids Struct. 38, 3251–3262.